Whisker-like Position Sensor for Measuring Physiological Motion

Özkan Bebek, *Student Member, IEEE,* M. Cenk Çavuşoğlu, *Senior Member, IEEE*

***Abstract*— This paper presents the design and characterization of a whisker-like three-dimensional position sensor. The whisker sensor is a flexible, high precision, high bandwidth contact sensor designed for measuring biological motion of soft tissue for medical robotics applications. Low stiffness of the sensor prevents damage on the tissue during its contact. Two different designs, one for measuring large displacements, the other for small displacements are described. Simulation and measurement results from prototype of both designs are reported.**

***Index Terms*— Flexible structures, medical robotics, physiological motion sensing, three-dimensional sensor, whisker-like.**

I. Introduction

Physiological motions are measured and actively compensated during robotic-assisted medical interventions to improve the accuracy of the surgery [1]–[8]. The sensors for measuring the physiological motion of the target tissue is a critical component of the overall robotic system. In this paper a whisker-like three-dimensional, high precision, high bandwidth, flexible contact position sensor is proposed for measuring the physiological motion of the body in medical robotics applications. The proposed highly sensitive sensor equipped with micro strain gauges comes out from the tip of a manipulator and touches the tissue or skin surface. The whisker sensor can be in continuous contact with the point of interest, in contrast to other available sensors for measuring biological motion. It can be in continuous contact with the point of interest, in contrast to other available sensors for measuring biological motion. Its high precision and high resolution enables the robotic system to actively compensate for the relative motion between the surgical site and the surgical instruments.

Details about the system concept and related work in literature are presented in Section II. Design specifications of the sensor is provided in Section III. Section III-B describes the use of strain gauges for position measurement. In Section III-C, mechanics of the flexure beams are modeled. Final element analysis and experimental results of the proposed designs are given in Sections IV and V.

Manuscript submitted on December 7, 2007; revised May 1, 2008.

This work was supported in part by the National Science Foundation under Grants CISE IIS-0222743, EIA-0329811, and CNS-0423253, and in part by the US DoC under grant TOP-39-60-04003.

Ö. Bebek and M. C. Çavuşoğlu are with the Department of Electrical Engineering and Computer Science of Case Western Reserve University, Cleveland, OH 44106, USA (e-mail: oxb6@case.edu, cavusoglu@case.edu). Phone:+1-216-368-4575, Fax:+1-216-368-6039.

This paper was presented in part at the IEEE Int'l Conf. on Robotics and Automation, Rome, Italy, 2007.

II. System Concept and Use of Sensors

In robotic tele-surgery conventional surgical tools are replaced with robotic instruments which are under direct control of the surgeon through teleoperation. During off-pump coronary artery bypass graft (CABG) surgery, the robot arm and the robotic surgical instruments track the heart and breathing motion, which are the main sources of the physiological motions observed. The relative motion between the surgical site and the surgical instruments is canceled. As a result, the surgeon operates on the heart as if it were stationary, while the robotic system actively compensates for the relative motion of the heart. A typical heartbeat motion is in the order of 1-2 Hz with 12 mm maximum peak displacement [4]. Measurement of heart motion with high precision and high confidence is required for precise motion canceling performance. Also, redundant sensing systems are desirable for safety reasons.

Earlier studies in canceling beating motion with robotic-assisted tools used vision based and ultrasound based sensory systems to measure heart motion. Nakamura *et al.* [1] tracked heart motion with a 4-DOF robot using a vision system. The tracking error due to the camera feedback system was relatively large (error in the order of few millimeters in the normal direction) to perform beating heart surgery. Thakral *et al.* used a laser range finder system to measure one-dimensional motion of a rat's heart [2]. Groeger *et al.* used a two-camera computer vision system to measure local motion of heart and performed analysis of measured trajectories [3], and Koransky *et al.* studied the stabilization of coronary artery motion afforded by passive cardiac stabilizers using three-dimensional digital sonomicrometry [9]. Hoff *et al.* measured the beating heart motion in three dimensions using two 2-axis accelerometers [10], showing that acceleration measurements can reveal patterns that may be an indication of heart circulation failure. Ortmaier *et al.* [5] and Ginhoux *et al.* [6] also used camera systems to measure motion of the heart surface for their estimation algorithms. Cavusoglu *et al.* used a sonomicrometry system to collect heart motion data from an adult porcine [11], and they showed the feasibility of a robotic system performing off-pump coronary artery bypass grafting surgery. Vitrani *et al.* used ultrasound based visual imaging to guide a surgical instrument within the heart during surgery [12]. Bader *et al.* [13] estimated a portion of organ surface motion using a pulsating membrane model with a stereo vision system. The model was used to estimate the periodic organ motion when the camera view is occluded. Noce *et al.* [14] simulated a method that characterizes heart surface texture to detect heart motion with recorded sequences by a monocular vision system.

The experimental results indicate that vision sensors were not satisfactory for tracking in beating heart surgery. Vision systems have problems with noise and occlusions. Noise can be reduced by using fluorescent markers, but the occlusion problem remains significant, and is an important setback, especially during surgical manipulations. Although some research was directed towards estimating heart motion when the image was occluded [5], [13], a sensor that provides persistent position information is necessary for satisfactory tracking, i.e., a continuous contacting position sensor. Also the resolution of a vision system is restricted, depending on the camera quality and distance to the point of interest. Vision sensors can provide high precision measurements in tangential directions, but their precision is low in the normal direction.

Inertial sensors are not suitable for stand-alone use in position measurements, due to drift problems. Laser proximity sensors are limited to one dimensional measurement and can not provide any information about tangential motion of the heart surface. Cagneau *et al.* [7] used a force sensor equipped robot designed for minimally invasive surgery [15] to compensate for physiological motions in surgical tasks involving tissue contact. However the proposed force feedback controller did not perform effective motion compensation.

A sensor that is in continuous contact with tissue is necessary for satisfactory tracking. The continuous contact sensors used in measuring the heart motion in the current literature are limited to sonomicrometer. A sonomicrometric position sensor has been the sensor of choice in the earlier studies of this research, but obtaining precise position measurements is essential in closed loop control for tracking the beating heart. Although sonomicrometric sensors are very accurate, they contain noise from ultrasound echoes. Also, they are more prone to error in calibration between the base sensors and the robotic manipulator coordinate frame.

The whisker sensor that is introduced in this study is a high sensitivity, flexible, three-dimensional position sensor equipped with micro strain gauges. Because of the sensors resemblance to projecting hairs or bristles, which come out from the tip of the surgical manipulator and touch the heart surface, the sensor is called a whisker sensor. Sensors for different scopes were developed within the general whisker sensor description given above. Berkelman *et al.* [16] designed a miniature force sensor with strain gauges to measure forces in three dimensions at the tip of a microsurgical instrument. Two sets of crossed beams are used as the elastic elements of the force sensor. Scholz and Rahn [17] used an actuated whisker sensor to determine the contacted object profiles for underwater vehicles. This whisker sensor predicted contact point based on the measured hub forces and torques with planar elastica model. Solomon and Hartmann [18] used artificial whiskers to sense the profile of three-dimensional objects. They used an array of flexible steel wires fixed to bases equipped with four strain gauges to measure the two orthogonal components of the base moment. From the rate of change of moment, they calculated the radial contact distance and constructed the detected object's profile.

The next section of the paper focuses on the mechanical design of the proposed whisker sensor.

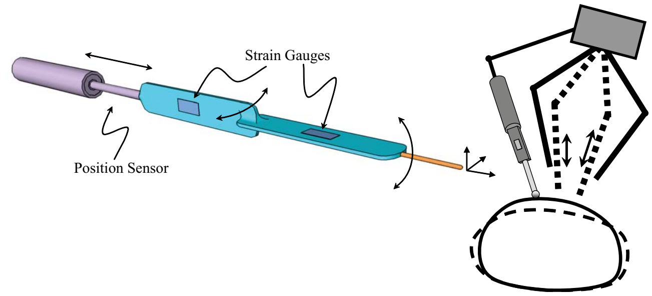

Fig. 1. Whisker Sensor Design 1. *Left*: One linear position sensor and two orthogonally placed flexure beams with strain gauges are used to measure the three-dimensional position of the sensor tip. *Right*: Sensor is attached to the manipulator base to provide continuous contact even when the surgical tools are not in close proximity, and to measure the heart position.

III. Whisker Sensor Design

The scope of this work is to create a miniature whisker sensor to measure the position of point of interest on the tissue or skin during medical interventions. Physically a whisker sensor is a long thin, and flexible extension used to detect the surrounding objects as well as their position, orientation and profiles. Design limitations include size constraints to make the tool usable in minimally invasive operations. The resolution of the sensor needs to be in the range of 50 μm in order to track the beating heart using the control algorithm described in [4].

Two whisker sensor designs are proposed to be used in two different scenarios.

Design 1 employs a linear position sensor connected to two flexible cantilever beams that are attached orthogonally with a ridged joint. The one dimensional linear motion along the normal dimension of the tip is measured with the linear position sensor and the two dimensional lateral motion of the tip is measured with strain gauge sensors placed on the beams by separating the motion into its two orthogonal components (Figure 1). These kind of beam designs are used in flexure joint mechanisms [19]. The design shown in Figure 1 can be attached to the robotic manipulator base to provide continuous contact. Even though the surgical tools are not in close proximity to the heart the sensor is capable of measuring the biological motion. The operation range of the sensor is adjusted to fit the heart motion, 12 mm peak to peak max displacement [11].

Design 2 employs a cross shaped flexible structure at the back of the linear sensor, which allows the lateral motion on the tip to be measured by the strain in the legs of the cross structure (Figure 2). A similar cross-shaped structure design was used by Berkelman [16] to measure force/torque values of the sensor tip. One major difference is the higher stiffness of their design, which was intended for force sensing. In the second design, a smaller linear position sensor with a spring loaded coil is used, since a smaller operation range of 5 mm in each direction is aimed. Cross shaped whisker sensor design is manufactured in relatively smaller dimensions and it is planned to be used with the system in a slightly different way as a result of its smaller size. The sensor will be attached to the

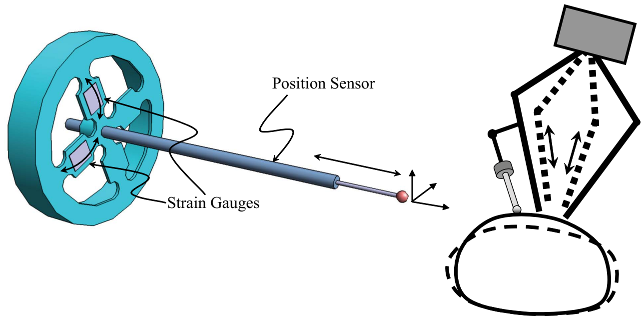

Fig. 2. Whisker Sensor Design 2. *Left*: One linear position sensor and a cross ($\times$) shaped flexible structure with strain gauges are used to measure the three-dimensional position of the sensor tip. *Right*: Sensor is attached to the robot arm to measure the displacement between the heart and the surgical tools.

surgical tool to measure the displacement between heart and surgical tools. The spring coiled position sensor will provide continuous contact with the tissue and give measurements with respect to the whisker base. The position of the point of interest will be estimated by the combination of the robot kinematics and the sensor measurements. This will bring more dexterity to the system, since the sensor base moves with the surgical tool.

Both of the proposed whisker sensor designs use a one axis linear position sensing element (i.e., a Linear Variable Displacement Transducer) and a two axes flexure strain gauge position sensor. The reason for using linear position sensors to measure the motion in the normal direction of the sensor is to provide low stiffness. The positions in the lateral axes are to be measured with strain gauges attached to flexure beams. Due to both designs' technological similarities, the same data acquisition system and similar models can be used to calculate the position of the sensor tip with respect to the sensor base. As mentioned earlier, similar geometrical designs are used in flexural joint mechanism designs [19]. Flexural joints are preferred because of the absence of friction and backlash. A drawback of the flexural elements is their limited deflection, which needs to be considered during the design.

Note that, due to the constraints of minimally invasive surgery, both of these designs will to be fitted inside a narrow cylindrical volume. The sensor design shown in Figure 1 is relatively bigger in size with respect the one shown in in Figure 2 since the linear transducer needs to support the flexure beams holding the strain sensors. This necessity for support requires a structurally stronger therefore bigger linear sensor. However, smaller linear sensors can be used in the design shown in Figure 2.

A. Equipment

As mentioned earlier, both designs require a one axis contactless linear position sensing element, and a two axes flexure beam strain gauge position sensing element. The following equipment were used to build prototype sensors.

Linear Position Sensors: MicroStrain 24 mm stroke Subminiature Differential Variable Reluctance Transducer (DVRT−or half bridge LVDT) was used for the measuring the displacement in the normal direction in Design 1. The sensor housing is 4.77 mm in diameter and made of 304 stainless steel. The sensor length is 132 mm at its maximum stroke. Resolution of the transducer is 5.7 μm with $\pm$ 1 μm repeatability.

MicroStrain 9 mm stroke Micro gauging DVRT with internal spring and bearings was used to measure the displacement in the normal direction in Design 2. Sensor housing is 1.80 mm in diameter and made of 304 stainless steel. The sensor's uncoiled length is 61 mm. Resolution of the transducer is 4.5 μm with $\pm$ 1 μm repeatability. Both sensors' response bandwidth is 7 kHz.

Strain Gauges: Kyowa KFG-5-120-C1-11L1M2R type strain gauges with nominal resistance value, $R_G = 119.6 \pm 0.4\ \Omega$ and gauge factor, $GF = 2.11 \pm 0.4$ are used with Design 1. Strain gauges are bonded with Instant Krazy Glue (Elmer's & Toagosei Company).

In Design 2 Micron Instruments SS-060-033-500PU-S4, semiconductor type strain gauges with nominal resistance value, $R_G = 540 \pm 50\ \Omega$ and gauge factor, $GF = 140 \pm 10$ are used. Strain gauges are bonded with Vishay Micro-measurement M-Bond 600 Adhesive Kit (M-Line Accessories Measurement Group) [20], [21].

Signal Conditioning Equipment: National Instruments PCI-6023E 12-Bit Multifunction DAQ Board, SCXI-1121 4-Channel Isolation Amplifier and SCXI-1321 Offset-Null and Shunt-Calibration Terminal Block were used to acquire strain gauge and LVDT measurements.

SCXI-1121 module has 4 channel input with internal half-bridge completion. Module was configured for a voltage excitation, V_{ex}, of 3.333 V. Input gains were adjusted to 1000 for Kyowa strain gauges and 10 for Micron Instruments strain gauges.

B. Strain Calculations

In order to minimize the effect of temperature changes and increase the sensitivity of the circuit, half-bridge configurations are used to measure strains. The strain, ε, is

$$\varepsilon = \frac{-2 \cdot (V_O - V_{O_{unstd}})}{GF \cdot V_{ex}} \cdot \left(1 + \frac{R_L}{R_G}\right), \tag{1}$$

where V_O is the measured output when the beam is deflected (strained), $V_{O_{unstd}}$ is the initial, unstrained measurement and V_{ex} is the excitation voltage [22]. $V_{O_{unstd}}$ is adjusted to 0 V by offset nulling beforehand. Offset nulling circuitry is used to rebalance the bridge and it also eliminates the effects of lead resistance.

If R_G, R_L, GF and V_{ex} values are substituted into (1), the final strain equations for the sensor designs are

$$Design\ 1: \quad \varepsilon = -0.2905 \cdot V_O, \tag{2}$$

$$Design\ 2: \quad \varepsilon = -0.0043 \cdot V_O. \tag{3}$$

C. Mechanics of the Flexure Beams

Using the strain values calculated in the Section III-B, the position change of the tip of the sensor, (x_{tip}, y_{tip}), can be

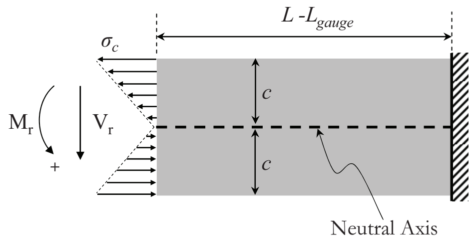

Fig. 3. Beam section forces and stresses at strain gauge position. σ_c is the normal stress acting on the surface of the transverse cross section. M_r is the resisting moment and V_r is the resisting shear force.

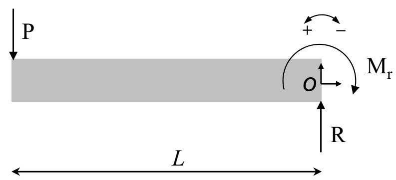

Fig. 4. Free body diagram of the cantilever beam. R is the reaction force at the supported end, M_r is the resisting moment and P is the bending force.

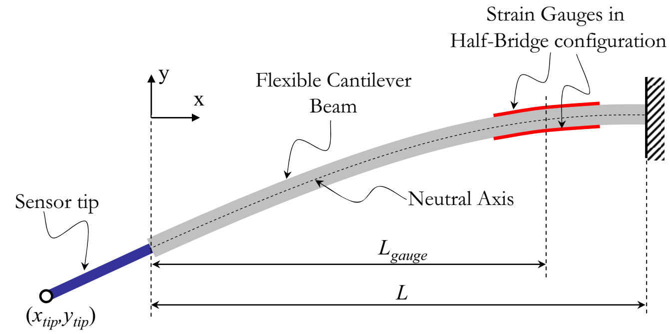

Fig. 5. Deflected Cantilever Beam.

found using basic mechanics of materials [23]. The following assumptions are made to model the mechanics:

1) The gravitational effects on the beam are negligible.
2) The deflection of the beam is in the elastic range.
3) The square of the slope of the beam, $\left(\frac{dy}{dx}\right)^2$, is negligible compared to unity, where $y = f(x)$ is the elastic curve.
4) The beam deflection due to shearing stress is negligible (a plane section is assumed to remain plane).
5) Young's modulus, E, and the second moment of the cross sectional area, I, values remain constant for any interval along the beam.

Design 1 - Cantilever Beam: The motion in the lateral plane of the flexure beams will cause two bending moments, M_x and M_y, in the sensor body. Bending moments can be calculated using the strain values, ε_x and ε_y, measured from the gauges attached on the cantilever beams. The strain and stress relation can be defined for linear elastic action with Hooke's law:

$$\sigma_x = E \cdot \varepsilon_x \tag{4}$$

where σ_x is the normal stress on a cross sectional plane and ε_x is the longitudinal strain. The normal stress will be maximum at the surface farthest from the neutral axis ($\sigma_{max} = \sigma_c$ at $y = c$ and c is half of the beam thickness, d). The normal stress at the surface, σ_c (Figure 3), can be calculated from the strain measurement of the surface using Hooke's Law as given in (4).

For the cantilever beam design, resisting moment at supported end is given as

$$M_r = -\frac{\sigma_c \cdot I}{c} = -\frac{\varepsilon_c \cdot E \cdot I}{c} \ . \tag{5}$$

The resisting moment acting at the point of strain gauge can be calculated using

$$M_r(L_{gauge}) = P \cdot L_{gauge} \ , \tag{6}$$

where P is the force acting on the unsupported end of the beam (Figure 4). Then, (5) can be rewritten as

$$P = -\frac{\varepsilon_c \cdot E \cdot I}{L_{gauge} \cdot c} \ . \tag{7}$$

During straight beam loading in an elastic action, the centroidal axis of the beam forms a curve defined as the elastic curve, $y = f(x)$. The differential equation for the elastic curve of the beam is

$$M(x) = E \cdot I \cdot \frac{d^2y}{dx^2} \tag{8}$$

where the moment, $M(x)$ is a function of x,

$$M(x) = P \cdot x \quad , \quad 0 \le x \le L \ . \tag{9}$$

If (8) is integrated twice, elastic curve can be derived. Beam's end point deflection, $y = 0$ at $x = L$, and end point slope, $\frac{dy}{dx} = 0$ at $x = L$, can be used as boundary conditions for the integration. Deflection curve and slope on the beam are given respectively as

$$y = -\frac{\varepsilon}{3 \cdot d \cdot L_{gauge}} \cdot (x^3 - 3 \cdot L^2 \cdot x + 2 \cdot L^3) \tag{10}$$

$$\frac{dy}{dx} = -\frac{\varepsilon}{d \cdot L_{gauge}} \cdot (x^2 - L^2) \ . \tag{11}$$

Then, slope of the tangent line at the end point of the cantilever beam ($x = 0$) is

$$\left.\frac{dy}{dx}\right|_{x=0} = \frac{\varepsilon \cdot L^2}{d \cdot L_{gauge}} \ . \tag{12}$$

It is assumed that sensor tip[1] has high modulus of elasticity (rigid) and its deflection is negligible. Therefore its contact position can be calculated using the following line equation.

$$y_{tip} = \left(\frac{\varepsilon \cdot L^2}{3 \cdot d \cdot L_{gauge}}\right) \cdot (3 \cdot x_{tip} - 2 \cdot L) \tag{13}$$

Design 2 - Cross Beam: Similar derivation methods can be used in this design. Motion of the position sensor tip in the lateral plane would cause two bending moments, M_x and M_y, on the cross flexure structure. Bending moments can be calculated using the strain values, ε_x and ε_y. Slope between the position sensor and the resting plane of the cross beam can be calculated using the measured strain.

[1]Sensor tip is a 15 mm long 303 stainless steel shaft with 1/16" diameter.

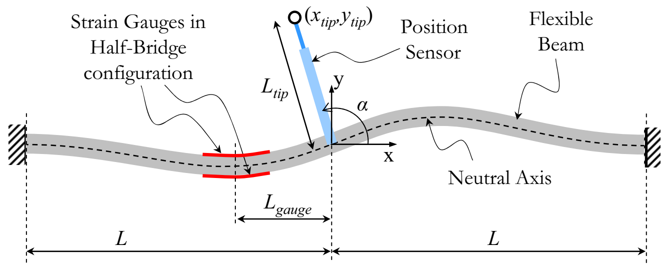

Fig. 6. Deflected Cross Beam Section.

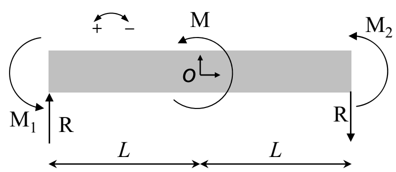

Fig. 7. Free body diagram of the cross beam section. R is the reaction force at the supported ends, M is the bending moment. M_1 and M_2 are the reaction moments at the supported ends.

Simplified free body diagram of the flexure cross section is shown in Figure 7. A relation between reaction forces and bending moment can be written as

$$R = \frac{3\ M}{4\ L}\ , \tag{14}$$

where R is reaction force at the supporting ends. Then, the resisting moment, M_r, acting at the point of the strain gauge is

$$M_r(-L_{gauge}) = \frac{M\ (2L - 3L_{gauge})}{4L}\ . \tag{15}$$

Using (5) and (15), the bending moment can be calculated as

$$M = -\frac{8\ \varepsilon_c EIL}{d(2L - 3L_{gauge})}\ . \tag{16}$$

The moment distribution on the beam with respect to position can be derived as,

$$M(x) = \frac{M\ (3x + 2L)}{4L}\ , \qquad -L \le x \le 0^- \tag{17a}$$

$$M(x) = \frac{M\ (3x - 2L)}{4L}\ , \qquad 0^+ \le x \le L\ . \tag{17b}$$

The beam's end point deflections, $y = 0$ at $x = -L$ and $y = 0$ at $x = L$, and end point slopes, $\frac{dy}{dx} = 0$ at $x = -L$ and $\frac{dy}{dx} = 0$ at $x = L$, can be used as boundary conditions for the integration of the elastic curve equation given below.

$$E \cdot I \cdot \frac{d^2y}{dx^2} = \frac{3Mx}{4L} + \frac{M}{2}\ , \quad -L \le x \le 0^- \tag{18}$$

Deflection curve and slope of the beam respectively are

$$y = -\frac{\varepsilon\ x\ (x+L)^2}{d(2L - 3L_{gauge})}\ , \quad -L \le x \le 0^- \tag{19}$$

$$\frac{dy}{dx} = -\frac{\varepsilon\ (x+L)\ (3x+L)}{d(2L - 3L_{gauge})}\ , \quad -L \le x \le 0^-, \tag{20}$$

and the slope of the tangent line at the base of the position sensor ($x = 0$) is

$$\left.\frac{dy}{dx}\right|_{x=0} = -\frac{\varepsilon L^2}{d\ (2L - 3L_{gauge})}\ . \tag{21}$$

Therefore, slope of the position sensor is

$$\left.\frac{dy_p}{dx_p}\right|_{x_p=0} = \frac{d\ (2L - 3L_{gauge})}{\varepsilon L^2} = \tan(\alpha)\ . \tag{22}$$

where

$$\left.\frac{dy_p}{dx_p}\right|_{x_p=0} \cdot \left.\frac{dy}{dx}\right|_{x=0} = -1\ . \tag{23}$$

Then, the angle of the position sensor with respect to the coordinate frame, α (Figure 6), is defined as

$$\alpha = \begin{cases} \tan^{-1}\left(\frac{d\ (2L - 3L_{gauge})}{\varepsilon L^2}\right), & \varepsilon > 0 \\ \tan^{-1}\left(\frac{d\ (2L - 3L_{gauge})}{\varepsilon L^2}\right) + \pi, & \varepsilon < 0 \\ \frac{\pi}{2}, & \varepsilon = 0 \end{cases} \tag{24}$$

It is assumed that components of the linear position sensor (housing and core) have high modulus of elasticity (rigid) and their deflection are negligible. Therefore its contact position can be calculated using the following equations.

$$\begin{aligned} x_{tip} &= L_{tip}\ \cos(\alpha) \\ y_{tip} &= L_{tip}\ \sin(\alpha) \end{aligned} \tag{25}$$

where L_{tip} is the overall length of the position sensor.

D. Resolution

The estimated ideal resolution of the sensors can be calculated using (2), (3), (13), (25) and the resolution of the DAC system. The calculated resolution of the Design 1 is $(x,\ y,\ z) = (10.1,\ 4.7,\ 5.7)\ \mu m$. The resolution difference in the x and y axes are due to the relative placement of the strain gauges to sensor tip and the length of flexures. Resolution of Design 2 is $(x,\ y,\ z) = (0.9,\ 0.9,\ 4.5)\ \mu m$, note that resolution of x and y axes are same due to symmetry of the design. This resolution estimate is valid for the ideal case and does not include the effects of noise and unmodeled nonlinear effects.

IV. Finite Element Simulation

Finite Element Model (FEM) analyses were done on the flexure beams to check the derived mathematical models (Figures 8 and 10). Parabolic tetrahedron mesh elements were used in the analyses. Flexure parts of the Design 1 and Design 2 FEMs had 18,220 and 135,029 degrees of freedom, respectively. Principal stress values (σ_{11}) were analyzed in the Finite Element Analysis (FEA) models. As the maximum stress on the surface of a deflected beam is equivalent to the principal stress value, corresponding strain values are calculated with principal stresses using Hooke's Law.

In this analysis, it was also confirmed that the effect of two-dimensional lateral motion on the flexure beams can be separated into its two orthogonal components with the used flexure geometries (cross structured beams and orthogonally fixed cantilever beams). This enabled the use of strain gauges for measuring motion in two dimensions.

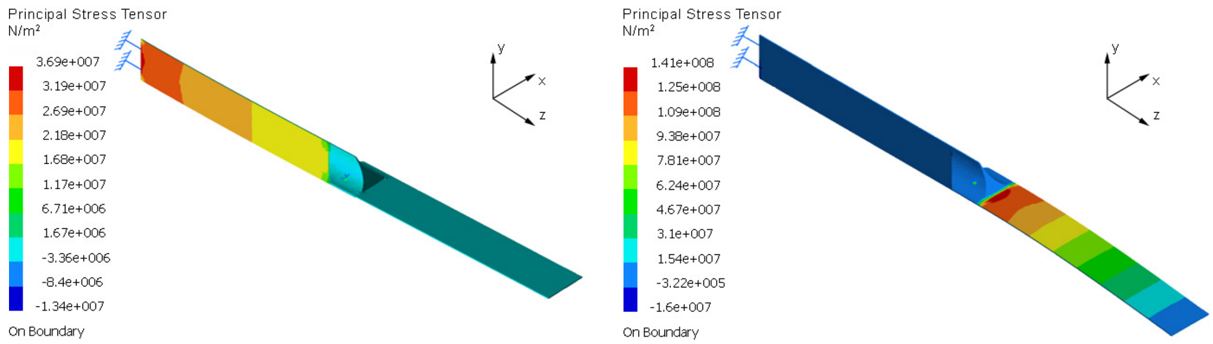

Fig. 8. FEA principal stress results of the flexure beam design. *Left* - Sensor tip displacement of 6 mm in the x-direction. Stress value at the strain gauge position is $2.60 \cdot 10^7$ N/m^2. *Right* - Sensor tip displacement of -6 mm in the y-direction. Stress value at the strain gauge position is $8.84 \cdot 10^7$ N/m^2.

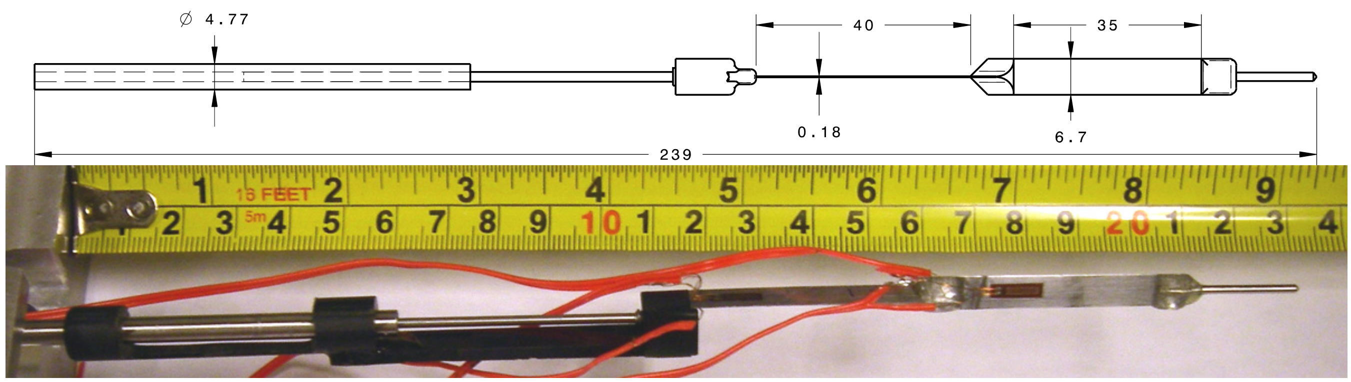

Fig. 9. Prototype of the Whisker Sensor Design 1. *Top* - Dimensions of the sensor prototype when the linear stage is fully extended are given (units in mm). *Bottom* - The sensor prototype is shown when the linear stage is fully extended. Overall length of the sensor when the linear stage is fully retracted and extended are 213 mm and 239 mm, respectively. The largest diameter of the prototype is 12.5 mm.

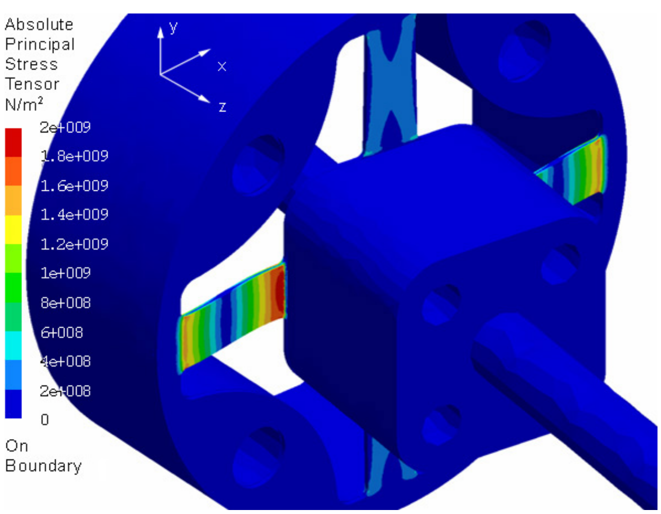

Fig. 10. FEA principal stress results of the cross flexure structure for a sensor tip displacement of -2.5 mm in the x-direction. Stress value at the strain gauge position is $4.18 \cdot 10^8$ N/m^2.

V. Experimental Results with the Prototypes

The prototypes of the designs are shown in Figures 9 and 11. Flexure parts are manufactured from cold rolled and annealed stainless steel sheets (E=193.2 GPa) with EDM wire cutting. The thickness of the sheets are $d_1 = 0.18\ mm$ and $d_2 = 0.15\ mm$ for Design 1 and Design 2, respectively. The second moment of the cross sectional areas are $I_1 = 3.14 \cdot 10^{-15}\ m^4$ and $I_2 = 4.50 \cdot 10^{-16}\ m^4$ for the given beam thicknesses.

The flexure parts of the prototypes are tested one axis at a time by measuring displacement of the sensor tip. The calibration of the sensors is done using a three-dimensional linear positioning stage. The calibration setup is depicted in Figure 12. Any error in the mathematical model was corrected using the calibration plots created with the collected data, as described below for each prototype.

Simulation and experimental strain and tip bending force measurement results of restrained sensor tip are given in Table I. In simulations, the estimated strain values are computed at a selected sensor tip displacement. For the experimental case, actual strain readings from the prototype sensor at the same tip deflection are reported. Strain values in the FEM analyses report the averaged strain values of the nodes where the actual strain gauges are bonded in the prototypes. If a small strain gauge is used with a relatively longer beam, the gauge is assumed to measure the strain value at the center point of the strain gauge. The measured strain value starts to deviate from the actual strain as the flexure beams get shorter relative to the length of the strain gauge. In the cantilever beam model, measured strain and the actual strain at the center point of the strain gauge can be assumed to be equal. But the effect of the mentioned centreline assumption can be observed with the experimental and the calculated values of the cross beam

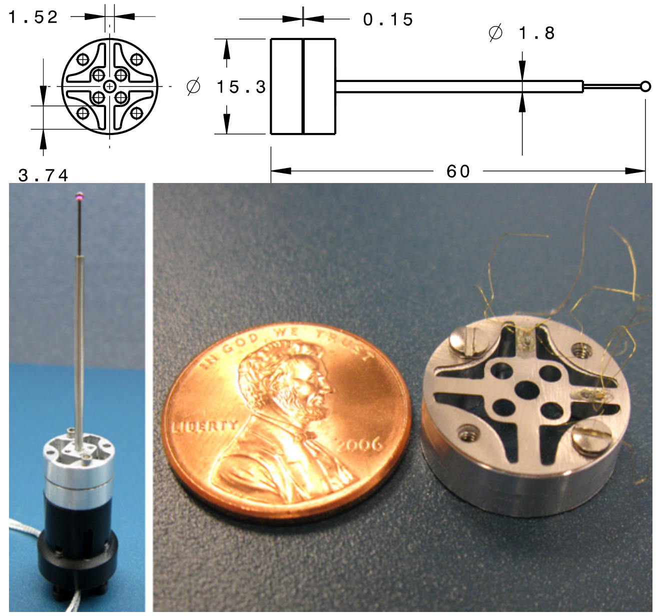

Fig. 11. Prototype of the Whisker Sensor Design 2: *Top* - Dimensions of the sensor prototype when the linear stage is uncoiled are given (units in mm). *Bottom Left* - Overall length of the sensor when the linear stage is uncoiled is 60.0 mm (as shown here). The largest diameter of the prototype is 15.3 mm. *Bottom Right* - Flexure part of the sensor shown next to a cent.

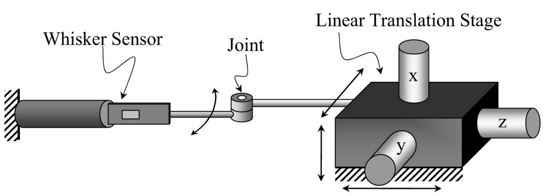

Fig. 12. Setup for static testing. A three-dimensional linear poisoning stage is used to move the sensor tip.

TABLE I

STRAIN AND TIP BENDING FORCE MEASUREMENT RESULTS FOR CONSTANT SENSOR TIP DISPLACEMENT: *In simulations, the estimated strain and tip bending force values at the selected sensor displacements are calculated. Actual strain gauge readings from the prototype sensors and measured tip force at the same tip displacements are reported for the experiment case.*

	Design 1		Design 2
Tip Displacement	6.0 mm		2.5 mm
Bending Flexure Element	X	Y	X or Y
Strain	m/m		
Mathematical Model	$2.38\ 10^{-4}$	$4.50\ 10^{-4}$	$1.60\ 10^{-3}$
Finite Element Analysis	$1.39\ 10^{-4}$	$4.58\ 10^{-4}$	$1.58\ 10^{-3}$
Experimental Value	$1.71\ 10^{-4}$	$4.49\ 10^{-4}$	$1.21\ 10^{-3}$
Tip Force	mN		
Mathematical Model	48.0	122.9	260.1
Experimental Value	12.2	58.7	694.4

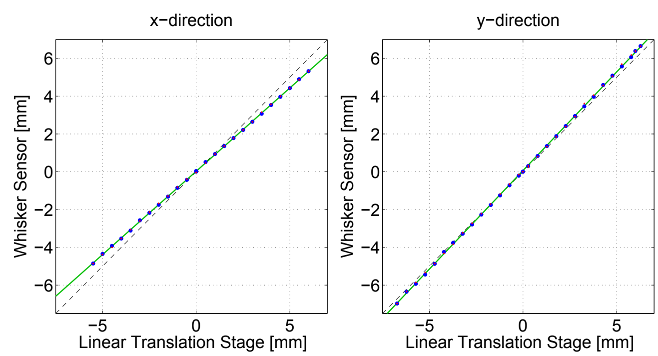

Fig. 13. Tip position measurement results for the prototype of the Whisker Sensor Design 1. $f(x) = 0.8819x + 0.0249$, $f(y) = 1.0433y + 0.0639$

prototype. Therefore the averaged strain values of the FEA nodes are tabulated in Table I. The estimates and actual strain values of cantilever beam sensor (Design 1) are closer than the values for the cross beam sensor (Design 2). Also, FEM results are affected by the deflection of sensor elements other than flexures (i.e., flexure joint elements, position sensors).

For tip force measurements, an ATI Nano17, 6-axis F/T sensor with force resolution of 1/160 N was used [24]. Measured and calculated force values were in the same order for both prototypes. The difference in the mathematical model is due to the estimation of the parameters such as E and I.

Prototype of Design 1: Figure 13 shows the static calibration data collected from the prototype of the Design 1. These plots show the general behavior of the sensors under predetermined sensor tip displacement. Linear fits to the data show that prototype of Design 1 has almost no nonlinearity. Especially the fit for y-direction data is almost on the theoretical line ($slope = \pi/4$). As the mechanical structure of the beams gets complicated, the reported results start to vary for the same element (Table I). For instance, reported results of the cantilever beam that measures the motion in y-direction are similar. This is mainly because of the geometrical simplicity of that element. Also, in the static testing no significant hysteresis is observed for this design.

Dynamic testing of the prototype under harmonic motion was conducted to determine the accurate working bandwidth of the sensors. A LVDT sensor attached to a motor was used to create harmonic motion at constant frequencies. The setup used for dynamic testing is depicted in Figure 14. Two dimensional position information collected from the 2 DOF dynamic setup is compared to the sensor's position output. Frequency response of the prototype of Design 1 is shown in Figure 16. The frequency response of the sensor is flat up to a resonance observed around 10 Hz. Phase difference is about 1-2 degrees in the 0.1-12.0 Hz range. Lissajous plots for the cantilever beam prototype under 0.1, 1.0 and 10.0 Hz harmonic motion is shown in Figure 15. Coefficient of determination (R^2) values obtained by least squares regression for the dynamic test results are shown in Figure 17-A. R^2 values are above 0.968 in the 0.1-10 Hz range for the prototype of

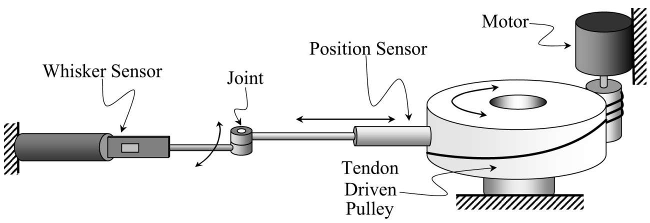

Fig. 14. Setup for dynamic testing. A tendon driven pulley is actuated with a servo motor to move the sensor tip.

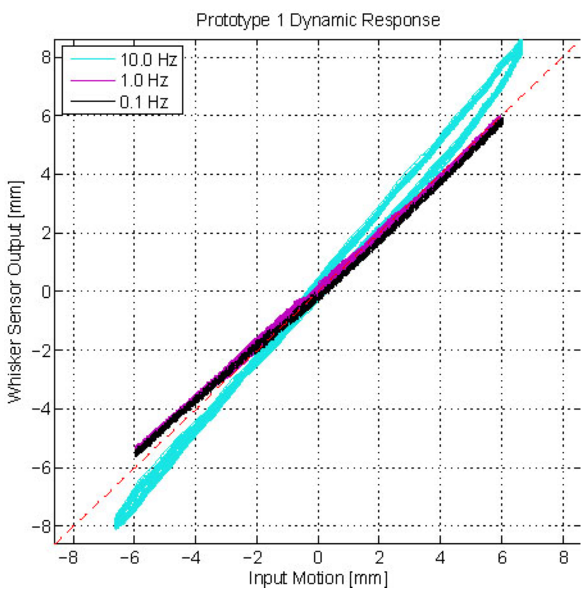

Fig. 15. Dynamic response data of the cantilever beam prototype under 0.1, 1.0 and 10.0 Hz harmonic motion.

Design 1, showing the linearity of the measurements collected by the sensor. Maximum measured percent hysteresis values are shown in Figure 17-B. Hysteresis values below 3% are observed for low frequencies, and around 6% hysteresis is observed for high frequencies.

Prototype of Design 2: Figure 18 shows the static calibration data collected from the prototype of the Design 2. No significant hysteresis was observed in the static testing of this design either. Cubic polynomial fits are shown in the plots. The nonlinearity observed in the Figure 18 is due to the measurement inaccuracies of the parameters used in (24) and (25). For subsequent tests, the measurements were corrected using the inverse of the cubic calibration curves. Two axes of the prototype are physically same, and similar response results are observed.

Frequency response of the Design 2 prototype is shown in Figure 20. The frequency response of the sensor is flat up to a resonance observed around 10 Hz. Phase difference is about 1-3 degrees in the 0.1-15.0 Hz range. Lissajous plots for the cross beam prototype under 0.1, 1.0 and 10.0 Hz harmonic motion is shown in Figure 19. Coefficient of determination (R^2) values are above 0.9608 in the 0.1-10 Hz range for the the prototype of Design 2, showing the linearity of the measurements collected by the sensor. Maximum measured hysteresis is around 5% for low frequencies. Smaller hysteresis values, around 3%, are observed for high frequencies.

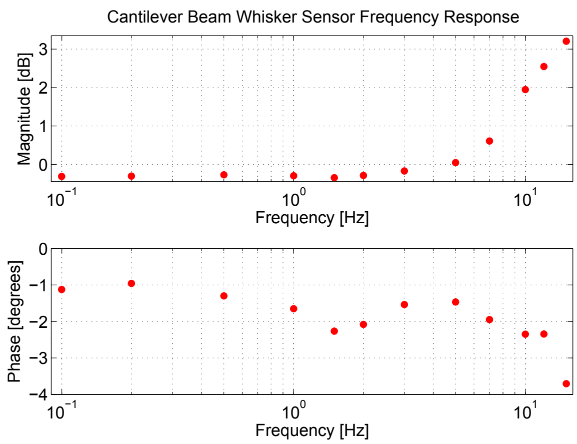

Fig. 16. Frequency response data of the cantilever beam prototype

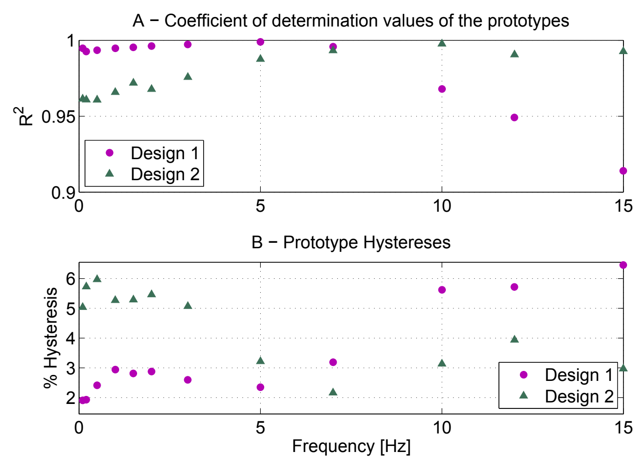

Fig. 17. A-Coefficient of determination values of the prototypes over the dynamic test bandwidth. B-Maximum measured percent hysteresis values of the prototypes over the dynamic testing bandwidth.

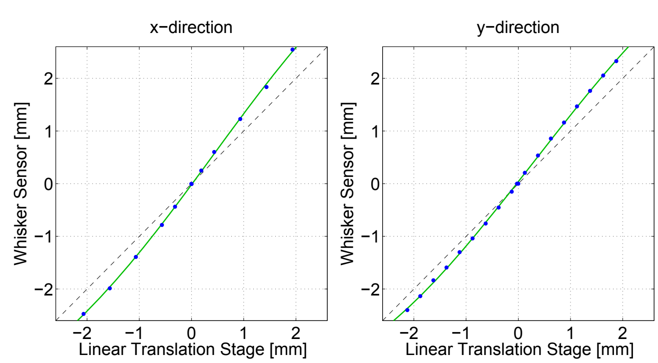

Fig. 18. Tip position measurement results for the prototype of the Whisker Sensor Design 2. $f(x) = -0.0211x^3 + 0.0245x^2 + 1.3375x - 0.0163$, $f(y) = -0.0197y^3 + 0.0188y^2 + 1.2622y + 0.0388$.

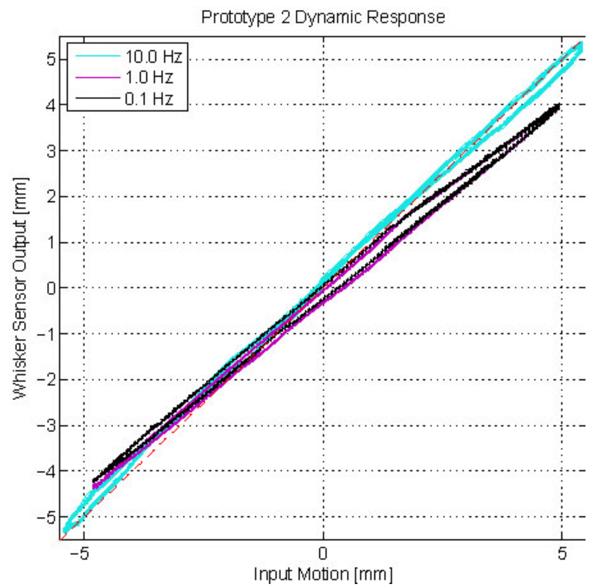

Fig. 19. Dynamic response data of the cross beam prototype under 0.1, 1.0 and 10.0 Hz harmonic motion.

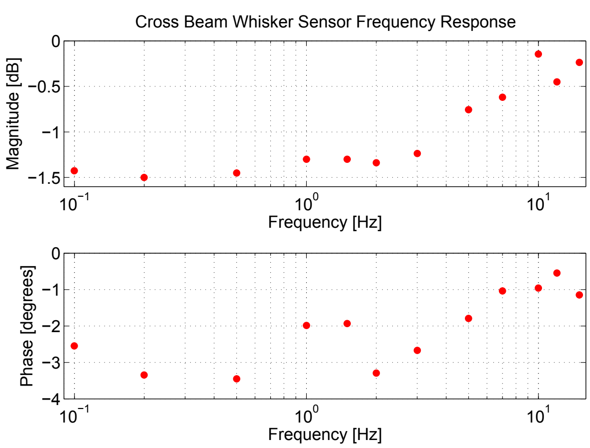

Fig. 20. Frequency response data of the cross beam prototype

Discussion & Conclusions

This paper presents a novel position sensor to measure physiological motion of biological tissue in robotic-assisted minimally invasive surgery. Two different designs are described, one for measuring large displacements, the other for small displacements. Design 1 can be attached to a robotic manipulator base to provide continuous contact. Even though the surgical tools are not in close proximity to the heart, the sensor is capable of measuring the biological motion. The operation range of the sensor is adjusted to fit the heart motion, which is 12 mm peak to peak max displacement. Design 2 has a smaller operation range of 5 mm in each direction. The sensor is manufactured in relatively smaller dimensions. This sensor will be attached to the surgical tool to measure the displacement between heart and surgical tools. The spring coiled position sensor will provide continuous contact with the tissue and give measurements with respect to the whisker base. This will bring more dexterity to the system. The manufactured prototypes showed that the use of proposed whisker sensors are promising and able to effectively measure dynamic motion at a bandwidth of 10 Hz.

Similar magnitude responses are observed in both sensor prototypes although their physical properties are different. Start of a resonant peak is visible in the magnitude plots. We believe that the resonance is caused by the dynamics of the two-degree-of-freedom test setup.

Coefficient of determination (R^2) values for Design 1 are higher for lower frequencies, while the opposite is true for Design 2 (Figure 17). The trend for hysteresis is roughly opposite for the designs. This is because of the fact that the hysteresis values depend on the bonding quality of the strain gauges to the flexure beams. Also, different strain gauges and different bonding adhesives are used in the two sensor prototypes. The R^2 values, however, depend on the sensors' accuracy. The accuracy is affected by the mechanics of the sensor, such as the precision of the static calibration as well as estimation of the parameters used in the calculations.

The resolution values reported in Section III-D are not homogenous in the three directions. If desired, the flexure beams' dimensions and the position of the strain gauges can be optimized to provide uniform resolution in every direction. The advantage of the presented flexure designs is their scalability to small dimensions. It is difficult to manufacture small joints or mechanisms to combine multiple position sensors to achieve low stiffness. Strain gauges are cost effective sensing elements compared to other designs that include multiple DVRTs and mechanisms.

References

[1] Y. Nakamura, K. Kishi, and H. Kawakami, "Heartbeat synchronization for robotic cardiac surgery," in *Proc. of IEEE International Conference on Robotics and Automation (ICRA)*, vol. 2, Seoul, Korea, May 2001, pp. 2014–2019.

[2] A. Thakral, J. Wallace, D. Tomlin, N. Seth, and N. V. Thakor, "Surgical motion adaptive robotic technology (S.M.A.R.T.): Taking the motion out of physiological motion," in *Proc. of 4th International Conference on Medical Image Computing and Computer-Assisted Intervention (MICCAI)*, Utrecht, The Netherlands, October 2001, pp. 317–325.

[3] M. Groeger, T. Ortmaier, W. Sepp, and G. Hirzinger, "Tracking local motion on the beating heart," in *Proc. of the SPIE Medical Imaging Conference*, vol. 4681 of SPIE, San Diego, CA, USA, February 2002, pp. 233–241.

[4] O. Bebek and M. C. Cavusoglu, "Intelligent control algorithms for robotic assisted beating heart surgery," *IEEE Trans. Robot.*, vol. 23, no. 3, pp. 468–480, June 2007.

[5] T. Ortmaier, M. Groeger, D. H. Boehm, V. Falk, and G. Hirzinger, "Motion estimation in beating heart surgery," *IEEE Trans. Biomed. Eng.*, vol. 52, no. 10, pp. 1729–1740, October 2005.

[6] R. Ginhoux, J. A. Gangloff, M. F. DeMathelin, L. Soler, J. Leroy, M. M. A. Sanchez, and J. Marescaux, "Active filtering of physiological motion in robotized surgery using predictive control," *IEEE Trans. Robot.*, vol. 21, no. 1, pp. 67–79, February 2005.

[7] B. Cagneau, N. Zemiti, D. Bellot, and G. Morel, "Physiological motion compensation in robotized surgery using force feedback control," in *Proc. of the International Conference on Robotics and Automation (ICRA)*, Rome, Italy, April 2007, pp. 1881–1886.

[8] C. Riviere, J. Gangloff, and M. de Mathelin, "Robotic compensation of biological motion of enhance surgical accuracy," *Proc. IEEE*, vol. 94, no. 9, pp. 1705–1716, September 2006.

[9] M. L. Koransky, M. L. Tavana, A. Yamaguchi, and R. Robbins, "Quantification of mechanical stabilization for the performance of offpump coronary artery surgery," in *Proc. of the Meeting of the International Society for Minimally Invasive Cardiac Surgery (ISMICS)*, Munich, Germany, June 2001, (Abstract).

[10] L. Hoff, O. J. Elle, M. J. Grimnes, S. Halvorsen, H. J. Alker, and E. Fosse, "Measurements of heart motion using accelerometers," in *Proc. of the Annual International Conference of the Engineering in Medicine and Biology Society (EMBC)*, vol. 3, San Francisco, CA, USA, September 2004, pp. 2049–2051.

[11] M. C. Cavusoglu, J. Rotella, W. S. Newman, S. Choi, J. Ustin, and S. S. Sastry, "Control algorithms for active relative motion cancelling for robotic assisted off-pump coronary artery bypass graft surgery," in *Proc. of the 12th International Conference on Advanced Robotics (ICAR)*, Seattle, WA, USA, July 2005, pp. 431–436.

[12] M.-A. Vitrani, H. Mitterhofer, G. Morel, and N. Bonnet, "Robust ultrasound-based visual servoing for beating heart intracardiac surgery," in *Proc. of the International Conference on Robotics and Automation (ICRA)*, Rome, Italy, April 2007, pp. 3021–3027.

[13] T. Bader, A. Wiedemann, K. Roberts, and U. D. Hanebeck, "Model-based motion estimation of elastic surfaces for minimally invasive cardiac surgery," in *Proc. of the International Conference on Robotics and Automation (ICRA)*, Rome, Italy, April 2007, pp. 2261–2266.

[14] A. Noce, J. Triboulet, and P. Poignet, "Efficient tracking of the heart using texture," in *Proc. of the Annual International Conference of the Engineering in Medicine and Biology Society (EMBC)*, Lyon, France, August 2007, pp. 4480–4483.

[15] N. Zemiti, G. Morel, T. Ortmaier, and N. Bonnet, "Mechatronic design of a new robot for force control in minimally invasive surgery," *IEEE/ASME Trans. Mechatronics*, vol. 12, no. 2, pp. 143–153, April 2007.

[16] P. J. Berkelman, L. L. Whitcomb, R. H. Taylor, and P. Jensen, "A miniature microsurgical instrument tip force sensor for enhanced force feedback during robot-assisted manipulation," *IEEE Trans. Robot. Autom.*, vol. 19, no. 5, pp. 917–922, October 2003.

[17] G. R. Sholz and C. D. Rahn, "Profile sensing with an actuated whisker," *IEEE Trans. Robot. Autom.*, vol. 20, no. 1, pp. 124–127, February 2004.

[18] J. H. Solomon and M. J. Hartmann, "Biomechanics: Robotic whiskers used to sense features," *Nature*, vol. 443, no. 7111, p. 525, October 2006.

[19] M. P. Koster, "Flexural joints in mechanisms," in *Proceedings of the ASME Dynamic Systems and Control Division*, vol. 2, 2000, pp. 855–859.

[20] "Surface preparation for strain gage bonding - application note B-129-8," Vishay Micro-Measurements, Shelton, CT, USA, Tech. Rep. 11129, Feburary 2005. [Online]. Available: http://www.vishay.com/doc?11129

[21] "Strain gage installations with M-bond 43-B, 600, and 610 adhesive systems - instruction bulletin B-130," Vishay Micro-Measurements, Shelton, CT, USA, Tech. Rep. 11130, April 2007. [Online]. Available: http://www.vishay.com/doc?11130

[22] "Strain gauge measurement - a tutorial," National Instruments, Austin, TX, USA, Tech. Rep. 078, August 1998.

[23] W. F. Riley, L. D. Sturges, and D. H. Morris, *Mechanics of Materials*, 5th ed. New York, USA: John Wiley & Sons Inc., 1999.

[24] ATI Industrial Automation, *Nano17, 6-axis Force/Torque Sensor*, ATI Industrial Automation Inc., Apex, NC, USA, 2008. [Online]. Available: http://www.ati-ia.com/products/ft/ft%5Fmodels.aspx?id=Nano17